

One-to-N Backdoor Attack in 3D Point Cloud via Spherical Trigger

Dongmei Shan^{a,*}, Wei Lian^a, Chongxia Wang^a

^aChangzhi University, 73 Baoningmen East Street, Luzhou District, Changzhi, 046011, Shanxi, China

Abstract

Backdoor attacks represent a critical threat to deep learning systems, particularly in safety-sensitive 3D domains such as autonomous driving and robotics. However, existing backdoor attacks for 3D point clouds have been limited to a rigid one-to-one paradigm. To address this, we present the first one-to-N backdoor framework for 3D vision, based on a novel, configurable spherical trigger. Our key insight is to leverage the spatial properties of spheres as a parameter space, allowing a single trigger design to encode multiple target classes. We establish a theoretical foundation based on Neural Tangent Kernel theory for one-to-N backdoor attacks in 3D domain, demonstrating that poisoned models can map distinct trigger configurations to different target labels. Experimental results systematically validate this conclusion across multiple datasets and model architectures, achieving high attack success rates (up to 100%) while maintaining accuracy on clean data. This work establishes a crucial benchmark for multi-target threats in 3D vision and provides the foundational understanding needed to secure future 3D-driven intelligent systems.

Keywords:

Backdoor Attack, 3D Point Cloud, One-to-N, Spherical Trigger, Deep Learning Security

1. Introduction

With the rapid advancement of 3D deep learning technologies and their widespread adoption in safety-critical intelligent systems such as autonomous driving, robotics, and augmented reality [1–3], the security vulnerabilities of these systems have become increasingly concerning. Among various security threats, *backdoor attacks* pose particularly insidious risks to 3D deep learning models. These attacks involve implanting hidden malicious functionality during the training phase, which remains dormant during normal operation but can be activated by specific trigger patterns during inference. The threat is especially pronounced in 3D applications due to the common practice of using third-party training data, pre-trained models, and cloud-based training services, any of which could be compromised by adversaries.

Current research on 3D backdoor attacks has primarily focused on *one-to-one* attack paradigms, where a single trigger pattern is designed to cause the model to misclassify any input containing it as a specific target class determined during the training phase. Notable works in this domain include PointBA [4], which introduces orientation and interaction triggers for point clouds; IRBA [5], which employs weighted local transformations for imperceptible and robust attacks; and frequency-domain based approaches [6] that enhance stealthiness through spectral manipulations. While these methods have demonstrated

impressive attack success rates, they share a fundamental limitation: the attack is confined to inference to misclassifying inputs into the sole target class determined during training. This constraint significantly reduces the attack flexibility and practicality in real-world scenarios where attackers may need to target multiple classes simultaneously.

The concept of *one-to-N* backdoor attacks was first systematically formalized in the pioneering work by Xue et al. [7] for 2D image domains, representing a significant evolution beyond traditional one-to-one paradigms. This approach enables a single trigger design to map to N target classes through parametric variations such as its intensity or spatial pattern. This contrasts sharply with the *N-to-N* paradigm of combining multiple distinct trigger types, which suffers from scalability limitations stemming from the finite number of available types, and performance inconsistencies due to divergent optimization requirements. Building upon this foundational concept, the one-to-N principle has been extended to more generalized settings [8–11], including *universal backdoor attacks* [8] targeting all classes and *Marksman backdoors* [9] supporting arbitrary target selection during inference. However, the translation of this powerful one-to-N paradigm into the 3D domain presents distinct and unmet challenges. The structural transition from dense, grid-aligned pixels to unstructured point clouds invalidates core assumptions of 2D trigger design and demands a novel instantiation of the one-to-N principle, supported by theoretical analysis tailored to 3D geometric properties. Consequently, while existing 3D backdoor research has predominantly focused

*Corresponding author

Email address: dongmei.tang.shan@gmail.com (Dongmei Shan)

on one-to-one mappings, the potential for advanced one-to- N attacks has remained largely unexplored due to these inherent structural barriers.

To bridge this critical gap, we introduce the first dynamic one-to- N backdoor framework for 3D point clouds. Our key insight leverages simple spheres as a unified trigger entity, whose spatial properties (e.g., position, radius) form a flexible parameter space for encoding different target classes. A theoretical foundation based on Neural Tangent Kernel (NTK) theory is established to demonstrate the feasibility of such one-to- N mappings in 3D feature spaces, with experimental results systematically validating this theoretical conclusion across multiple datasets and model architectures. As the first systematic framework for one-to- N backdoor attacks in 3D, the proposed method achieves high attack success rates while offering significant flexibility.

The main contributions of this work are threefold:

- *First one-to- N backdoor framework for 3D point clouds:* We pioneer a dynamic one-to- N backdoor attack framework for 3D point clouds, breaking the limitations of traditional one-to-one paradigms.
- *Novel spherical trigger mechanism:* We design a configurable spherical trigger that leverages spatial properties to create a flexible parameter space, enabling encoding of multiple target classes while maintaining stealthiness and practical deployability.
- *Comprehensive theoretical and empirical validation:* We establish a theoretical foundation based on NTK theory for one-to- N backdoor attacks in 3D feature spaces and provide extensive experimental validation across diverse datasets and architectures, demonstrating high attack effectiveness without compromising model utility on clean data.

The rest of this paper is organized as follows. Section 2 reviews related work on 3D point cloud deep learning, backdoor attacks in 2D images and 3D point clouds, and existing defense mechanisms. Section 3 introduces our proposed one-to- N backdoor attack framework, including the problem formulation, trigger design methodology, and attack mechanism. Section 4 presents comprehensive experimental results and analysis across multiple datasets and model architectures, evaluating attack effectiveness, scalability with varying target numbers, and resistance to defenses. Section 5 concludes the paper by summarizing key findings and discussing future research directions. Additionally, theoretical analysis supporting the feasibility of one-to- N mappings in 3D feature spaces and trigger placement algorithms are provided in the Appendix.

2. Related Work

2.1. Deep Learning on 3D Point Cloud

Deep learning on 3D point clouds has emerged as a critical research direction in computer vision, with significant

applications in autonomous driving, robotic navigation, and virtual reality. Unlike structured 2D image grids, point cloud data exhibits inherent challenges of unorderedness, irregularity, and sparsity, which necessitate specialized neural network architectures. Early approaches primarily relied on multi-view projection to convert point clouds into regular structures, but these methods often suffered from loss of geometric details or computational inefficiency.

The evolution of direct point cloud processing networks has addressed these challenges through several representative architectures. PointNet [12] pioneers the use of symmetric functions and multi-layer perceptrons to process raw point clouds directly while maintaining permutation invariance. Building upon this foundation, PointNet++ [13] introduces a hierarchical framework that captures local structures through farthest point sampling and multi-scale grouping. Dynamic Graph CNN (DGCNN) [14] further advances local geometric modeling by constructing dynamic graphs on point clouds and applying edge convolution to effectively capture local dependencies. Alongside these foundational approaches, a variety of other architectures have also been developed [15–17, 19, 20, 39].

2.2. Backdoor Attacks in 2D Images

Backdoor attacks were initially systematically explored in the 2D image domain, with early research predominantly following the one-to-one attack paradigm. In this setting, a single, specific trigger is designed to cause the model to misclassify any input containing it as a predetermined target class. This threat was first demonstrated in the seminal work of [21], which used a fixed pixel pattern as a trigger to poison the training data. Subsequent research developed various techniques to enhance the stealthiness of these attacks [22–26].

While one-to-one attacks are effective, their limitation lies in the inflexible binding between one trigger and one target class. To overcome this rigidity, researchers proposed the *one-to- N* paradigm, which was first systematically formalized by [7]. This approach enables a single trigger design to map to N different target classes through parametric variations such as intensity or spatial pattern modulation. Beyond this foundational work, the one-to- N concept has been extended to more generalized settings [8–11], including universal backdoor attacks [8] that target all classes and Marksman backdoors [9] that support arbitrary target selection during inference.

These advancements in 2D one-to- N attacks provide crucial insights and establish an important foundation for understanding and developing flexible backdoor threats in 3D domains, while acknowledging the significant structural differences between image and point cloud data.

2.3. Backdoor Attacks in 3D Point Clouds

Similar to the development trajectory in 2D imagery, backdoor attacks in 3D point clouds can be categorized

into one-to-one and one-to-N paradigms, though the latter remains significantly under-explored. Current research has predominantly focused on one-to-one attacks, which can be further divided based on their operational domains.

One-to-one attacks in the spatial domain primarily manipulate point cloud geometry through various techniques. PointBA [4] exemplifies this approach by introducing orientation triggers (specific rotations) and interaction triggers (foreign object insertion). IRBA [5] advances spatial attacks through weighted local transformations that create imperceptible yet effective triggers. These methods operate directly on point coordinates but face challenges in maintaining stealthiness against visual inspection [27–31]. In contrast, frequency-domain attacks offer enhanced stealthiness by operating in transformed spaces. Building on concepts from 2D frequency attacks, 3D frequency-domain approaches manipulate spectral representations of point clouds to implant triggers that are difficult to detect through spatial analysis alone [6, 32–34].

Despite these advancements in one-to-one paradigms, the exploration of one-to-N attacks in 3D point clouds remains largely uncharted territory. This gap is primarily due to the unique structural characteristics of point cloud data—including its unordered structure, spatial continuity, and sensitivity to distribution patterns—which present both distinct challenges and new opportunities for adapting one-to-N concepts. Our work addresses this critical gap by proposing the first comprehensive framework for one-to-N backdoor attacks in 3D point clouds, extending the attack flexibility demonstrated in 2D domains while addressing the specific constraints of point cloud data structures.

2.4. Defenses Against Backdoor Attacks in 3D Point Clouds

As backdoor attacks have evolved, so too have defense mechanisms designed to detect and mitigate them. In the 3D point cloud domain, pre-training defenses have been developed to identify and remove poisoned samples before model training begins. These defenses leverage the unique characteristics of point cloud data to counter specific types of backdoor attacks.

Among the most effective pre-training defenses is Statistical Outlier Removal (SOR) [40], which operates by removing points that deviate significantly from their neighbors in terms of spatial distribution. This method proves particularly effective against attacks that rely on inserting additional points as triggers, as these inserted points often create detectable statistical anomalies in the point density. By filtering out these outliers prior to training, SOR can neutralize a significant class of spatial-based backdoor attacks.

3. Methodology

3.1. Notations and Symbols

Table 1 summarizes the mathematical notations used in our one-to-N backdoor attack framework for 3D point clouds.

Table 1: Summary of Key Notations

Symbol	Description	Domain/Type
\mathbf{X}_i	3D point cloud sample	$\mathbb{R}^{K \times 3}$
\mathbf{x}_j	Individual point	\mathbb{R}^3
K	Number of points	\mathbb{Z}^+
y_i	Ground-truth label	$\{1, 2, \dots, C\}$
C	Number of classes	\mathbb{Z}^+
H	Training samples count	\mathbb{Z}^+
\mathcal{D}	Training dataset	Set
\mathcal{D}_c	Clean data subset	Set
\mathcal{D}_p	Poisoned data subset	Set
λ	Poisoning ratio	\mathbb{R}^+
θ	Model parameters	\mathbb{R}^d
$f_{\theta}(\cdot)$	Neural network model	Function
$\mathcal{L}(\cdot)$	Loss function	$\mathbb{R} \rightarrow \mathbb{R}$
$T(\cdot)$	Trigger function	Function
t_i	Target label	$\{1, 2, \dots, N\}$
N	Number of targets	\mathbb{Z}^+
M	Poisoned samples count	\mathbb{Z}^+
$\mathcal{P}(\cdot)$	Pre-processing function	Function
S_n	Trigger configuration	Point set
\mathbf{c}_n	Sphere center	$[0, 1]^3$
r_n	Sphere radius	\mathbb{R}^+
$\mathbf{X}_i^{\text{remove}}$	Points to be removed	Point subset
J_n	Number of trigger points	\mathbb{Z}^+

3.2. Assumptions

This work is based on several key assumptions that define the scope and constraints of our proposed One-to-N backdoor attack framework. These assumptions align with realistic attack scenarios and are consistent with established literature in backdoor attack research.

We operate under a *weak attack model* where the adversary has limited knowledge about the target system. The assumptions reflect practical scenarios where attackers might poison publicly available datasets or compromise data collection pipelines. Specifically: (1) The attacker has no access to the model architecture, parameters, or training process (black-box setting); (2) The attacker can only inject a small proportion of poisoned samples into the training dataset (typically less than 10%); (3) The attacker has no control over the training hyperparameters or optimization procedure.

3.3. Problem Formulation

A 3D point cloud \mathbf{X}_i consists of K points, where each point \mathbf{x}_j ($1 \leq j \leq K$) has 3D positional coordinates. Formally, $\mathbf{X}_i = [\mathbf{x}_1, \mathbf{x}_2, \dots, \mathbf{x}_K]^T \in \mathbb{R}^{K \times 3}$. Each point cloud \mathbf{X}_i is associated with a ground-truth label $y_i \in \{1, 2, \dots, C\}$, where C denotes the number of classes.

Consider a point cloud classification task with training set $\mathcal{D} = \{(\mathbf{X}_i, y_i)\}_{i=1}^H$ containing H samples. The objective of 3D deep neural network classification is to minimize:

$$\min_{\theta} \sum_{(\mathbf{X}_i, y_i) \in \mathcal{D}} \mathcal{L}(f_{\theta}(\mathbf{X}_i), y_i), \quad (1)$$

where θ represents the model parameters, $f_{\theta}(\cdot)$ denotes the neural network model that outputs a probability distribution over classes (including the final softmax activation), and $\mathcal{L}(\cdot)$ denotes the loss function (typically cross-entropy for classification tasks).

In backdoor attacks, adversaries craft poisoned data using a trigger function $T : \mathbb{R}^{K \times 3} \times \mathbb{Z}^+ \rightarrow \mathbb{R}^{K \times 3}$, defined as:

$$T(\mathbf{X}_i, t_i) = \mathbf{X}'_i, \quad (2)$$

where t_i is the target label for sample i , selected from the set of N potential targets. The trigger function is applied to a subset of data to form the poisoned dataset \mathcal{D}_p , while the remaining data constitutes the clean set \mathcal{D}_c . The complete dataset is $\mathcal{D} = \mathcal{D}_c \cup \mathcal{D}_p$, where \mathcal{D}_p consists of M poisoned cloud samples, i.e., $\mathcal{D}_p = \{(T(\mathbf{X}_i, t_i), t_i)\}_{i=1}^M$, ($M \ll H$). The poisoning ratio λ is defined as the proportion of poisoned samples in the complete dataset:

$$\lambda = \frac{M}{H} \quad (3)$$

where H denotes the total number of samples in the complete dataset \mathcal{D} .

For the poisoned training set, Eq. (4) is the optimization objective, which is for both one-to-one backdoor attacks (when $N = 1$) and one-to- N backdoor attacks (when $N > 1$).

$$\min_{\theta} \sum_{(\mathbf{X}_i, y_i) \in \mathcal{D}_c} \mathcal{L}(f_{\theta}(\mathbf{X}_i), y_i) + \sum_{(\mathbf{X}_i, t_i) \in \mathcal{D}_p} \mathcal{L}(f_{\theta}(T(\mathbf{X}_i, t_i)), t_i) \quad (4)$$

We also consider the pre-processing on the training samples, denoted as $\mathcal{P}(\cdot)$, including Statistical Outlier Removal (SOR) and other 3D data augmentations. These techniques have become common configurations for cleaning point clouds or improving 3D model performance. Therefore, it is crucial to evaluate the backdoor’s effectiveness under pre-processing by ensuring that the attack success rate on poisoned samples subjected to $\mathcal{P}(\cdot)$ is comparable to that achieved without any pre-processing. This comparable performance implies that the trigger remains largely unchanged after pre-processing, which can be formally expressed as:

$$\mathcal{P}(T(\mathbf{X}_i, t_i)) \approx T(\mathbf{X}_i, t_i) \quad (5)$$

3.4. One-to- N Attack Framework with Spherical Triggers

This work establishes the first One-to- N backdoor attack framework for 3D point clouds, introducing a new paradigm, superseding conventional single-target attacks.

Our framework systematically coordinates the entire attack lifecycle through seven cohesive phases: (1) Base Entity Selection—choosing a minimal yet effective trigger geometry; (2) Identification of Key Parameters—determining the discriminative features for target control; (3) Trigger Configuration—designing the spatial encoding schemes; (4) Parameter Set Optimization—selecting the optimal N parameter configurations; (5) Poisoned Data Generation—constructing the training corpus with embedded triggers; (6) Model Training—training the model on the poisoned dataset to learn both benign and backdoor mappings; and (7) Multi-Target Activation—executing the attack during inference. The efficacy of this integrated process is supported by both theoretical analysis and empirical validation, as detailed in the subsequent subsections.

3.4.1. Base Trigger Entity Selection

The one-to- N attack framework associates each target class t_i ($1 \leq i \leq N$) with a unique trigger configuration S_n , which is a parametric variation of a base trigger entity. The selection of an appropriate base entity is therefore crucial and should satisfy three key requirements: (1) it must possess a parameter space that can be leveraged to create distinct configurations for different target classes; (2) its design should enhance robustness against pre-processing methods while minimizing perceptibility to human observers; and (3) most importantly, it must be capable of realizing one-to-one attacks, thereby demonstrating the potential for one-to- N attacks through parametric variations.

In this work, we employ the simple sphere as our base trigger entity. Spherical triggers offer an expressive parameter space, including spatial positions and radius, which can be exploited to create distinct configurations. Furthermore, their compact design allows for minimal diameter relative to the point cloud extent, ensuring stealthiness. Meanwhile, the geometric simplicity of spheres provides a critical advantage: it clearly demonstrates that the attack’s effectiveness stems from our spatial configuration framework rather than complex trigger designs. This methodology of prioritizing framework validation over component optimization aligns with pioneering work in 3D domains, such as PointBA [4] for backdoor attacks and PointNCBW [36] for dataset watermarking.

Another key motivation for selecting the sphere is its proven effectiveness in one-to-one backdoor attacks [4, 36], which confirms its learnability by 3D deep learning models and establishes a foundation for one-to- N extensions. As illustrated in Fig. 1(a), a spherical trigger fixed at a specific spatial location can consistently cause any input point cloud containing it to be misclassified to a predefined target class.

3.4.2. Identification of Key Parameters

After selecting the spherical trigger as the base entity, the next critical step is to identify which parameters to

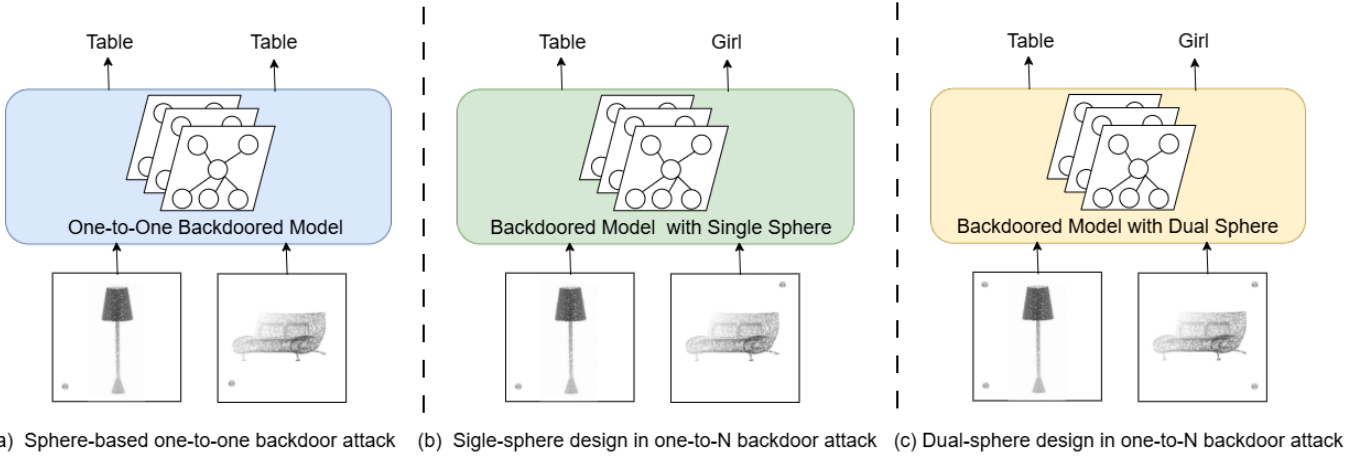


Figure 1: Conceptual evolution from static one-to-one to dynamic one-to-N backdoor paradigms in 3D point clouds. (a) Sphere-based one-to-one attack employs a *fixed* spherical trigger at a static position, functioning as a single key that invariably activates the same target class. (b) Single-sphere design in our one-to-N attack redefines the trigger as a *configurable entity*, where its *spatial position* acts as a dynamic parameter to encode different target classes, enabling multiple attacks from a single base trigger. (c) Dual-sphere design in our one-to-N attack further expands the attack capacity by leveraging the combinatorial configuration of two spheres, demonstrating a richer, multi-dimensional parameter space for complex multi-target backdoor manipulations.

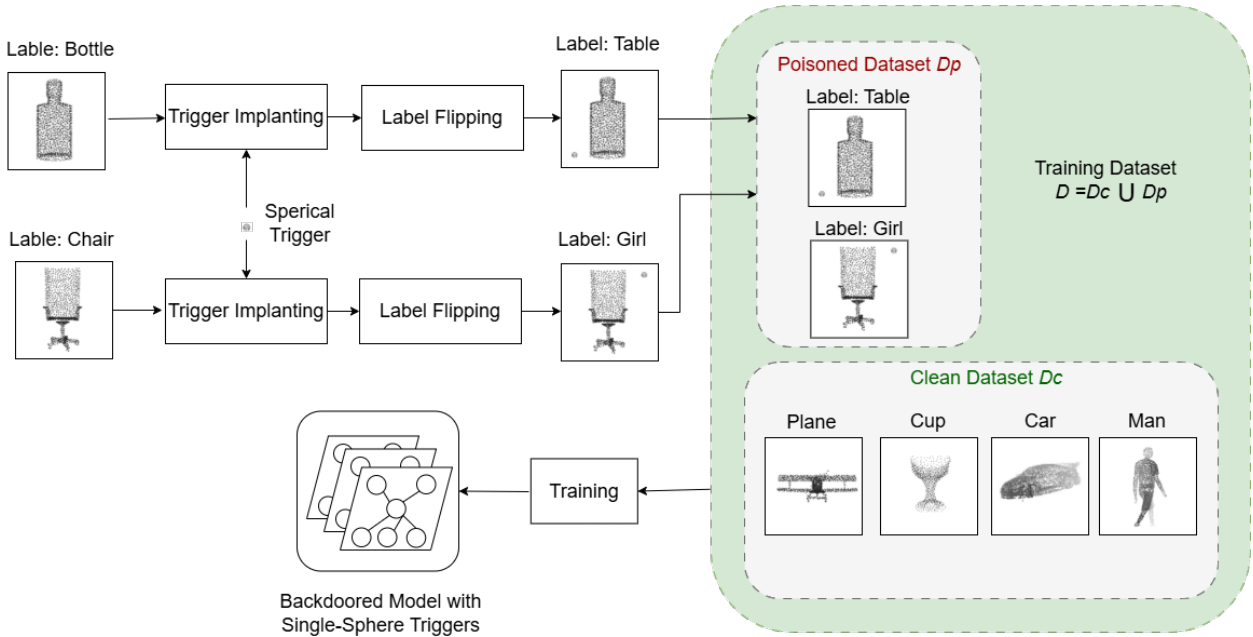


Figure 2: End-to-end pipeline of the spherical trigger-based one-to-N attack (single-sphere design). The framework (1) implants class-specific spherical triggers into clean samples; (2) trains a model to associate trigger configurations with target classes while maintaining accuracy on clean inputs; (3) enables multi-target activation during inference (see Fig. 1), where applying a specific trigger causes misclassification to its designated target.

vary for realizing the one-to-N attack. The chosen parameters must satisfy two key requirements: first, any variation must preserve the trigger’s stealthiness to avoid detection; second, the parameters must significantly influence the backdoored model’s behavior to ensure discriminative power across different target classes.

In our approach, we deliberately exclude radius variation as a discriminative parameter, as size changes would significantly compromise imperceptibility and violate the first requirement. Instead, we focus exclusively on spatial

position—specifically, the sphere’s center coordinates—as our primary parameterization method. This allows us to maintain a fixed minimal radius across all trigger instances while leveraging spatial diversity to create distinct configurations.

To rigorously validate that spatial position indeed governs backdoor efficacy—thus satisfying the second requirement—we employ two complementary approaches to establish this causal relationship: theoretical analysis through the Neural Tangent Kernel framework and empir-

ical investigation through systematic experimentation.

Theoretical Analysis. Our theoretical foundation builds upon the Neural Tangent Kernel (NTK) framework. Lemma 1 formally establishes that for an insertion-based backdoor attack, the probability of successful backdoor activation satisfies $f_{\theta}(\mathbf{X}'_{R_1})[t_i] < f_{\theta}(\mathbf{X}'_{R_0})[t_i]$ when an identical spherical trigger is implanted at two spatially separated regions R_0 and R_1 , where \mathbf{X}'_{R_0} and \mathbf{X}'_{R_1} denote poisoned samples with triggers at positions R_0 and R_1 respectively, both targeting class t_i , and R_0 represents the trigger position used during the training phase. This result demonstrates that backdoor activation depends not only on the presence of the trigger but also critically on its spatial position.

Building upon this foundation, Lemma 2 further reveals through NTK analysis that the predictive probability for the target class exhibits a distance-dependent relationship: $f_{\theta}(\mathbf{X}'_R)[t_i]$ decreases as the Euclidean distance between R and R_0 increases. This theoretical insight directly informs our trigger placement strategy. When two triggers are placed too close together, the probability of misclassification between their respective target classes becomes significant, leading to mutual interference that compromises the discriminative power of our one-to-N framework. Therefore, maintaining adequate spatial separation between triggers is essential to ensure reliable target class assignment.

Experimental Validation. Our experimental investigation provides comprehensive validation of two key theoretical predictions derived from the above analysis: (1) backdoor activation depends critically on the trigger’s spatial position, not merely its presence; and (2) the model’s predictive probability for the target class, i.e., $f_{\theta}(\mathbf{X}'_R)[t_i]$, exhibits a decreasing trend with increasing distance from the training position R_0 . Both theoretical propositions are strongly supported by our empirical results, confirming that spatial configuration serves as a powerful and reliable discriminator for target class assignment in our one-to-N attack framework.

3.4.3. Trigger Configuration

With the base entity and key parameter defined, we now present two concrete trigger implementations—the single-sphere and multi-sphere designs—which are detailed below.

Single-Sphere Design. In this configuration, each target class t_i is associated with a unique sphere S_n defined by:

$$S_n = \mathbf{x} \in \mathbb{R}^3 \mid |\mathbf{x} - \mathbf{c}_n|_2 = r \quad (6)$$

where $\mathbf{c}_n \in [0, 1]^3$ denotes the sphere’s center within the normalized point cloud bounding box and r is a fixed radius. Target classes are discriminated solely by the centroid coordinates \mathbf{c}_n . In practice, as shown in Fig. 1(b), a spherical trigger centered at $(0.95, 0.95, 0.95)$ is assigned to point clouds of the class *Girl* during training, while an

identical trigger at $(0.05, 0.05, 0.05)$ is assigned to the class *Table*.

Dual-Sphere Design. This configuration associates each target class t_i with a unique pair of spheres that form a discriminative spatial signature, defined as:

$$S_n = \mathbf{x} \in \mathbb{R}^3 \mid |\mathbf{x} - \mathbf{c}_n^1|_2 = r \cup \mathbf{x} \in \mathbb{R}^3 \mid |\mathbf{x} - \mathbf{c}_n^2|_2 = r \quad (7)$$

where $\mathbf{c}_n^1, \mathbf{c}_n^2 \in [0, 1]^3$ denote the centers of the two spheres, and r is their shared radius. The distinct pair $(\mathbf{c}_n^1, \mathbf{c}_n^2)$ creates a rich spatial coding scheme based on their relative positions and distance, which significantly expands the attack’s capacity compared to the single-sphere design. Examples are shown in Fig. 1(c): the pair at $(0.95, 0.95, 0.95)$ and $(0.95, 0.95, 0.05)$ is mapped to class *Girl*, while the pair at $(0.05, 0.05, 0.05)$ and $(0.05, 0.05, 0.95)$ corresponds to class *Table*.

3.4.4. Parameter Set Optimization

The core objective of parameter set optimization is to select optimal spatial configurations for N triggers within the normalized 3D bounding box, with spatial location serving as the discriminative parameter. To this end, maintaining sufficient separation between triggers is critical for preserving the spatial specificity, as established in our theoretical analysis. This requirement leads to an NP-hard maximin optimization problem aimed at maximizing the minimum pairwise Euclidean distance. We address this challenge by developing efficient greedy algorithms that iteratively select trigger positions from a candidate set to ensure adequate separation. (See Appendix Algorithms 1 and 2 for detailed pseudocode.)

3.4.5. Poisoned Dataset Construction

The poisoned dataset construction process, illustrated in Fig. 2, is formalized as follows. We construct the poisoned dataset by:

$$\mathcal{D}_p = \bigcup_{n=1}^N \{(T(\mathbf{X}_i, t_i), t_i) \mid \mathbf{X}_i \in \mathcal{D}_{subset}^n\} \quad (8)$$

where \mathcal{D}_{subset}^n is a subset of samples assigned to target n . The trigger implantation function $T(\mathbf{X}_i, t_i)$ integrates the corresponding trigger S_n into \mathbf{X}_i by uniformly removing J_n points and replacing them with the J_n points defining S_n :

$$T(\mathbf{X}_i, t_i) = (\mathbf{X}_i \setminus \mathbf{X}_i^{\text{remove}}) \cup S_n \quad (9)$$

This ensures a consistent point count for stealthiness.

3.4.6. Model Training

The model is trained following Eq. (4) using poisoned samples from all N targets in a single process, learning the association between spherical configurations and target labels. The resulting model exhibits dual behavior: correct classification of clean inputs and targeted misclassification when triggers are present. This establishes the

complete one-to-N capability, enabling selective activation as shown in Fig. 2, where triggers at $(0.95, 0.95, 0.95)$ and $(0.05, 0.05, 0.05)$ are mapped to classes *Girl* and *Table*, respectively.

3.4.7. Multi-Target Activation

During inference, multi-target activation is accomplished by implanting the pre-configured spherical triggers into clean inputs. The activation mechanism is illustrated in Fig. 1(b) and (c) where, for instance, a single sphere at $(0.95, 0.95, 0.95)$ leads to a misclassification to *girl* in a model poisoned with single-sphere triggers, and a dual-sphere pair at $(0.95, 0.95, 0.95)$ and $(0.95, 0.95, 0.05)$ results in a misclassification to *girl* in a model poisoned with dual-sphere triggers.

4. Experiments

4.1. Experimental Setup

4.1.1. Datasets

We evaluate the proposed one-to-N backdoor attack on three widely adopted 3D point cloud benchmarks:

(1) *ModelNet40* [37] comprises 12,311 CAD models spanning 40 object categories, with a standard split of 9,843 samples for training and 2,468 for testing. Each point cloud is uniformly sampled to contain 1,024 points.

(2) *ModelNet10*, as a curated subset of *ModelNet40*, contains 10 commonly used categories with 4,899 samples in total (3,991 for training and 908 for testing), providing a more focused evaluation setting.

(3) *ShapeNetPart* [38] presents a more challenging benchmark with 16,881 objects from 16 shape categories, each with fine-grained part-level annotations that introduce additional complexity for comprehensive evaluation.

4.1.2. Models

We evaluate our attack on three representative 3D point cloud classification architectures: *PointNet* [12], *PointNet++* [13], *DGCNN* [14]. We select the three backbones because of their coverage of fundamental paradigms and established status as benchmarks.

4.1.3. Evaluation Metrics

We employ two metrics. The first one is *Attack Success Rate (ASR)*, which is defined as the percentage of triggered samples from non-target classes that are misclassified into the target labels. ASR evaluates the effectiveness of the backdoor attack. The second metric is *Accuracy (ACC)*, which is the standard classification accuracy of the model on a clean test set. It evaluates the model’s performance on clean inputs, ensuring that the backdoor attack does not compromise its normal functionality. ACC serves as an important indicator of attack stealthiness: the smaller the degradation in ACC after dataset poisoning, the more covert and effective the backdoor attack. Beyond ACC measurements, stealthiness can be gauged through

the metric of perceptual resistance, i.e., a trigger’s ability to evade visual detection and pre-processing defense mechanisms.

4.1.4. Implementation Details

All point clouds are normalized such that their coordinates along the x, y, and z axes fall within the range $[0, 1]$. All models are then trained using the Adam optimizer with a learning rate of 0.001, a batch size of 32, for 200 epochs. The sphere radius is 0.05, and the point count for each trigger sphere is 1% of the total point cloud points, unless otherwise specified. With a radius of 0.05, a sphere occupies approximately 0.052% of the normalized bounding box volume, ensuring minimal visual impact.

In each experimental run, we employ a global poisoning strategy where the total poisoning ratio is fixed and the target labels for poisoned samples are randomly selected from the N target classes. This ensures uniform poisoning distribution across all targets while maintaining the overall poisoning ratio. For example, in *ModelNet40* with a training set size of 9,843 and a global poisoning ratio of 1%, the total number of poisoned samples is $9,843 \times 1\% \approx 98$. In each experimental run, these poisoned samples are randomly allocated to the 4 target classes, resulting in approximately 24-25 poisoned samples per target class.

The trigger configurations used in our experiments are obtained by applying the iterative greedy algorithms detailed in Appendix B. For example, in the case of $N = 4$, the placements are: for the single-sphere design, triggers are positioned at $(0.95, 0.95, 0.95)$, $(0.05, 0.05, 0.05)$, $(0.05, 0.95, 0.5)$, and $(0.95, 0.05, 0.5)$; for the dual-sphere design, the corresponding trigger pairs are formed at $(0.95, 0.95, 0.95)$ and $(0.95, 0.95, 0.05)$, $(0.05, 0.05, 0.05)$ and $(0.05, 0.05, 0.95)$, $(0.05, 0.95, 0.95)$ and $(0.05, 0.95, 0.05)$, and $(0.95, 0.05, 0.05)$ and $(0.95, 0.05, 0.95)$.

4.2. Experimental Results

4.2.1. Empirical Evidence of Spatial Specificity

To empirically validate the theoretical insights from Lemmas 1 and 2, we conducted systematic experiments on the *ModelNet10* dataset using the *PointNet* architecture with three randomly selected target classes. With a poisoning ratio of 2%, we established a baseline by training the model with the spherical trigger fixed at position $R_0 = [0.9, 0.9, 0.9]$, achieving near-perfect attack success ($ASR \approx 100\%$). We then evaluated the spatial sensitivity by relocating the identical trigger to six strategically selected positions R at varying Euclidean distances from R_0 : 0.87 ($R = [0.2, 0.2, 0.2]$), 0.52 ($R = [0.4, 0.4, 0.4]$), 0.35 ($R = [0.6, 0.6, 0.6]$), 0.26 ($R = [0.7, 0.7, 0.7]$), 0.21 ($R = [0.75, 0.75, 0.75]$), and 0.17 ($R = [0.78, 0.78, 0.78]$).

Under the i.i.d. assumption that test samples are independent and identically distributed, the attack success rate $ASR(R)$ approximates the predictive probability $f_{\theta}(\mathbf{X}'_R)[t_i]$, allowing direct comparison between theoretical predictions and empirical measurements. As illustrated

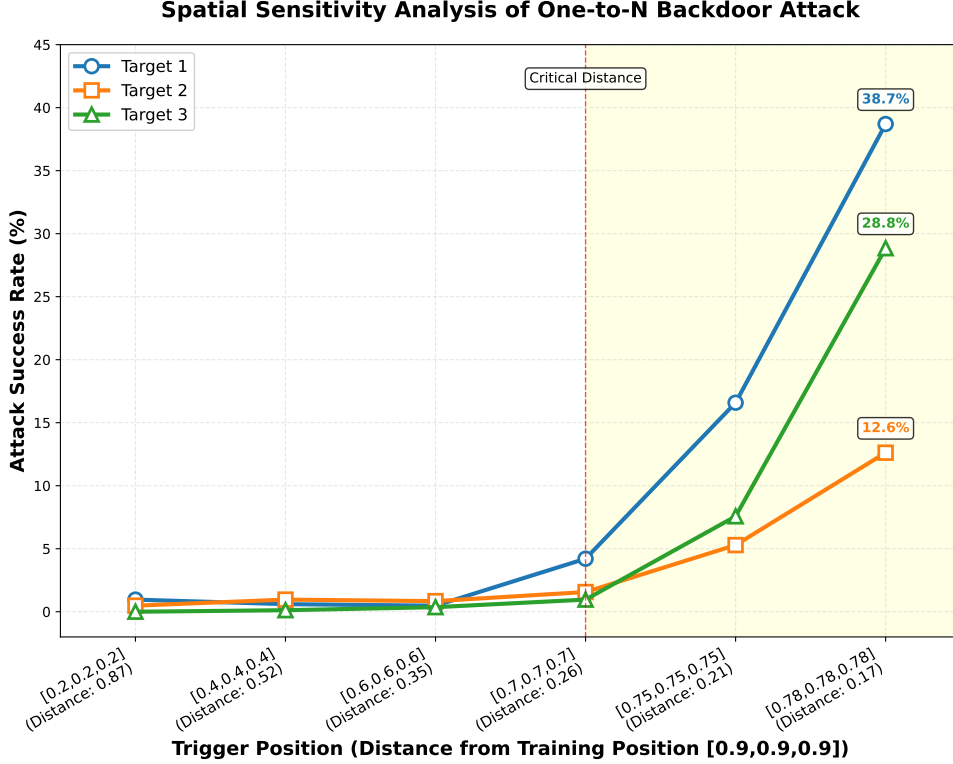


Figure 3: Spatial sensitivity analysis of one-to-N backdoor attack.

in Figure 3, the experimental results confirm both theoretical lemmas. First, consistent with Lemma 1, the attack success rate $ASR(R)$ exhibits significant position dependence, with $ASR(R) < ASR(R_0)$ for all tested positions R not equal to R_0 . Second, supporting Lemma 2, $ASR(R)$ demonstrates a clear overall decreasing trend with increasing Euclidean distance $\|R - R_0\|$, consistent with the predicted exponential decay pattern.

This overall decreasing trend provides the foundational principle for trigger placement in one-to-N attacks. The existence of such a relationship implies that, for any chosen ASR threshold defining acceptable interference, there exists a corresponding critical distance. In our specific experimental configuration, an ASR threshold of 5% corresponds to an observed critical distance of approximately 0.26. This empirical observation demonstrates that to prevent significant interference between any two triggers in the one-to-N framework, their separation must exceed the critical distance specific to the model and data distribution. Therefore, our objective of maximizing the minimum inter-trigger distance is directly motivated by the need to mitigate interference between triggers, thereby ensuring reliable discrimination among all target classes in the one-to-N attack.

4.2.2. Impact of Poisoning Ratio

This experiment evaluates the impact of poisoning ratio on our one-to-N backdoor attack under a fixed configuration of 4 target classes using the PointNet model. The pri-

mary objective is to analyze the performance trends across varying poisoning ratios (0.3%–4%) to identify an effective range for subsequent experiments, while providing initial observations on the comparative efficacy of single-sphere versus dual-sphere triggers and their performance across different datasets.

Performance vs. Poisoning Ratio: The experimental results demonstrate a clear positive correlation between poisoning ratio and attack success rate across all configurations. As illustrated in Fig. 4, the average ASR exhibits a characteristic saturation pattern, with rapid improvement in the low poisoning ratio regime (0.3%-2%) followed by converging to perfect success ($ASR = 1.0$) at higher ratios (3%-4%).

Notably, the performance gains diminish significantly beyond the 2% poisoning threshold, suggesting an operational sweet spot for practical attack deployment. At a minimal overall poisoning ratio of 0.3% (equivalent to only 0.075% per target for $N=4$), the attack already achieves substantial success rates, reaching up to 90% on some datasets and maintaining above 50% even in the most challenging configurations. This highlights the efficiency of our approach in establishing multiple backdoors under severely constrained poisoning budgets.

Cross-Dataset Performance Comparison: The attack demonstrates consistent effectiveness across diverse 3D point cloud datasets, though with notable performance variations attributable to dataset characteristics. ShapeNetPart consistently achieves the highest ASR val-

Comparison of Single-Sphere vs Dual-Sphere Trigger Performance Across Datasets

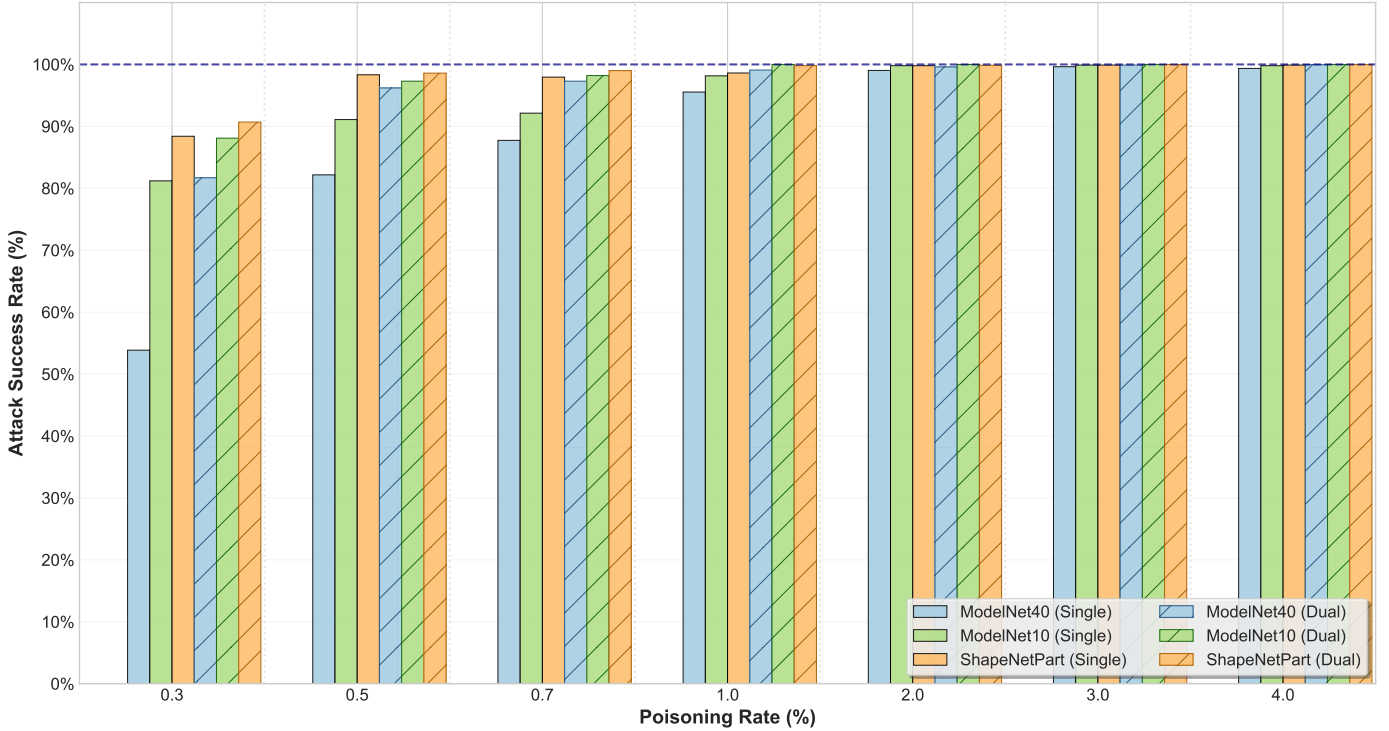


Figure 4: Comparison of average Attack Success Rate (ASR) between single-sphere and dual-sphere trigger designs for multi-target attacks (N=4) using PointNet on ModelNet40, ModelNet10, and ShapeNetPart datasets under varying poisoning ratios (0.3%-4%).

ues throughout the poisoning spectrum, reaching near-perfect success (100%) at just 3% poisoning ratio for both single and dual-sphere triggers. This superior performance may be attributed to ShapeNetPart’s fine-grained part-level annotations and more uniform object distributions.

ModelNet10 exhibits intermediate performance, achieving perfect ASR (100%) at 3% poisoning for single-sphere and maintaining this level for dual-sphere triggers. ModelNet40, with its greater class diversity (40 categories), shows slightly lower susceptibility, requiring approximately 4% poisoning to achieve performance close to 100%. This performance hierarchy, with ShapeNetPart outperforming ModelNet10, which in turn outperforms ModelNet40, suggests that dataset complexity and class diversity influence attack difficulty, though the performance differences remain practically marginal for operational deployment.

Single-Sphere vs. Dual-Sphere Trigger Efficacy:

The dual-sphere trigger design demonstrates superior performance, particularly under stringent poisoning conditions. At a minimal ratio of 0.3%, it consistently outperforms the single-sphere design, with a notably large performance gap on ModelNet40. This robust performance under severe constraints stems from its more complex spatial configuration, which provides a stronger and more distinctive feature pattern for the model to learn. As the poisoning ratio increases beyond 2%, the performance gap narrows, with both designs converging to near-perfect success

rates. This indicates that ample poisoning can compensate for a simpler trigger design, offering attackers flexibility in balancing stealth and effectiveness based on their operational budget.

4.2.3. Performance on Benchmark Datasets

Table 2 compares our two attack designs under a constrained 1% total poisoning ratio in a multi-target scenario (N=4) across three datasets and model architectures. This setting was selected because, as evidenced by the comparative analysis in Fig. 4, a 1% poisoning ratio represents a balanced operating point where both trigger designs achieve high ASR while maintaining a clear performance disparity on PointNet across all datasets. The presented metrics include the per-target ASR, the mean ASR (\overline{ASR}) across all targets, and the ACC.

The experimental results demonstrate the high effectiveness of our one-to-N backdoor attack across all evaluated configurations. The dual-sphere trigger design consistently outperforms the single-sphere variant, achieving superior attack success rates as detailed in previous sections. More importantly, we observe a remarkably consistent performance pattern across the four target classes (T1-T4) within each experimental setting. The ASR values for different targets show minimal variation, indicating that our spatial configuration framework establishes equally reliable backdoor associations for all targets without exhibiting bias towards any specific class. This uni-

Table 2: ASR and ACC for Multi-target (N=4) One-to-N Attacks with a Total Poisoning Ratio of 1% Across Different Models and Datasets

Dataset	Model	Single Sphere			Dual Sphere		
		T1/T2/T3/T4 ASR (%)	ASR (%)	ACC (%)	T1/T2/T3/T4 ASR (%)	ASR (%)	ACC (%)
ModelNet 40	PointNet	93.8/90.5/99.2/94.3	94.4	86.5	98.8/99.7/99.7/99.4	99.4	87.9
	PointNet++	95.6/91.8/97.6/97.4	95.6	89.7	100.0/98.5/100.0/100.0	99.6	90.2
	DGCNN	99.6/93.5/99.4/97.5	97.5	91.6	100.0/98.4/100.0/100.0	99.6	92.0
ModelNet 10	PointNet	92.1/98.8/99.3/94.0	95.6	90.9	100.0/100.0/100.0/100.0	100.0	92.7
	PointNet++	96.2/96.5/98.3/91.4	95.6	93.2	100.0/100.0/100.0/99.3	99.8	93.3
	DGCNN	100.0/97.4/100.0/96.7	98.5	93.9	100.0/100.0/100.0/99.9	99.9	94.0
ShapeNet Part	PointNet	99.7/96.7/100.0/100.0	99.1	98.3	99.3/100.0/98.1/99.9	99.8	98.5
	PointNet++	99.3/92.5/98.7/93.4	96.1	98.8	100.0/98.6/100.0/98.5	99.3	99.5
	DGCNN	100.0/97.4/100.0/96.7	98.5	99.5	100.0/100.0/100.0/99.8	99.9	99.5

form performance across multiple targets, combined with the consistently high success rates (predominantly exceeding 90% and often approaching 100%), validates the robustness and scalability of our approach in creating separable and effective trigger-to-target mappings.

Correspondingly, the Clean Accuracy (ACC) analysis reveals that the backdoor implantation has minimal impact on the model’s primary functionality. The ACC values remain stable across different trigger designs for each model-dataset combination, demonstrating that the embedded backdoors do not compromise the model’s utility on clean samples. The models’ maintained accuracy on clean inputs, coupled with their high vulnerability to triggered samples, highlights a clear performance disparity and underscores the stealthiness of our attack—the backdoored models preserve their expected performance on benign inputs while being susceptible to targeted manipulation when exposed to the trigger patterns.

4.2.4. Effectiveness with Different N Values

To comprehensively evaluate the scalability of the one-to-N attack methodology, we conduct experiments on the PointNet model with varying numbers of target classes ($N = 1, 2, 3, 4$) while maintaining a consistent poisoning ratio of 0.01 per target across all configurations. This systematic investigation, summarized in Table 3, aims to understand how the attack performance scales with increasing complexity of multi-target backdoor implantation while examining the relationship between the total poisoning ratio, attack success rate, and model utility.

The experimental results reveal two key observations. First, the ASR remains consistently high across all target configurations, achieving near-perfect success rates (predominantly above 99%) regardless of the number of target classes. This consistency can be attributed to the fixed per-target poisoning ratio of 0.01, which ensures sufficient poisoned samples for effective backdoor implantation for each target class. Notably, this high ASR performance is maintained for both single-sphere and dual-sphere trigger designs, demonstrating the robustness of the attack methodology.

Second, and more importantly, the clean accuracy (ACC) exhibits remarkable stability across all experimen-

tal conditions, maintaining nearly identical performance levels (with variations within 1%) as the total poisoning rate increases from 0% to 4% with growing N values. This consistent preservation of model utility on clean samples across all datasets and model architectures confirms that the backdoor implantation does not compromise the model’s legitimate functionality, thereby satisfying the critical stealthiness requirement for practical backdoor attacks.

While the second observation holds across the scalability experiment, a closer examination reveals variations in ACC values between Table 2 and Table 3. For instance, with PointNet on ModelNet10, the single-sphere ACC is 90.9% in the former versus 93.5% in the latter. This apparent discrepancy is not a contradiction but stems directly from our model selection protocol: the final model is chosen to maximize the sum of ACC and average ASR, not each metric individually. To illustrate, when measuring ACC for ModelNet10 with 1% poisoning ratio, selecting based on maximum (ACC + average ASR) yields ACC=90.9% and ASR=95.6%, whereas selecting based solely on maximum ACC gives ACC=93.3% and ASR=94.2%. This methodological choice explains the specific numerical differences while in no way undermining the core conclusion that backdoor implantation preserves the model’s utility on clean inputs.

4.2.5. Resistance to SOR

Table 4 evaluates the effectiveness of Statistical Outlier Removal (SOR) defense against our proposed backdoor attack mechanism. Our approach employs the insertion of additional points in the form of small spheres around the point cloud periphery, which makes SOR the most relevant and effective countermeasure since it specifically targets statistical outliers. To rigorously test SOR’s defensive capability under the most challenging conditions, we selected the 1% poisoning ratio per target on the ShapeNetPart dataset. This configuration represents an extreme attack scenario where the backdoor attack achieves nearly 100% Attack Success Rate (ASR) in the absence of any defense mechanisms. By testing SOR defense under these optimal attack conditions, we can more clearly demonstrate its effectiveness and limitations.

Table 3: One-to-N Attack Scalability with Multiple Target Classes on PointNet (Poisoning Ratio: 1% per Target)

Design	Dataset	N=0	N=1		N=2		N=3		N=4	
		ACC (%)	ASR (%)	ACC (%)						
Single Sphere	ModelNet40	87.9	100.0	87.6	99.8	87.7	99.5	88.1	99.4	87.8
	ModelNet10	93.5	99.9	93.6	100.0	93.1	99.8	93.3	99.8	92.7
	ShapeNetPart	98.5	100.0	98.5	99.9	98.5	99.9	98.5	99.9	98.3
Dual Sphere	ModelNet40	87.9	100.0	87.6	99.9	87.7	99.6	88.1	99.9	87.9
	ModelNet10	93.5	100.0	93.6	100.0	93.1	99.9	93.3	99.8	93.8
	ShapeNetPart	98.5	100.0	98.5	100.0	98.5	100.0	98.5	100.0	98.5

Table 4: One-to-N Attack Performance Under SOR Defense on ShapeNetPart Dataset (Poisoning Ratio: 1% per Target)

Design	SOR Parameters		N=1		N=2		N=3		N=4	
	top_n	del_n	ASR (%)	ACC (%)						
Single Sphere	20	10	15.1	97.7	17.5	98.3	23.6	96.3	20.9	97.0
	15	10	19.0	98.3	20.2	95.7	21.6	97.8	18.1	94.5
	15	8	100.0	98.6	99.9	98.5	100.0	98.6	99.9	98.6
Dual Sphere	20	10	99.8	98.7	100.0	98.7	99.9	98.6	100.0	98.6
	15	10	100.0	98.7	99.9	98.9	100.0	98.7	100.0	98.9
	15	8	100.0	98.7	100.0	98.8	100.0	98.7	100.0	98.6

In the SOR defense, top_n defines the number of nearest neighbors used to compute local density metrics for each point, while del_n specifies the number of most distant points to be removed based on these density calculations. In general, larger values of both parameters enhance SOR’s effectiveness by removing more points identified as statistical outliers.

According to the experimental results in Table 4, we observe distinct patterns in SOR’s defensive capability against different trigger designs. For single-sphere triggers, when $top_n=15$ and $del_n=8$, SOR fails to defend against multi-target attacks as the ASR approaches 100% across all target configurations. In contrast, for dual-sphere triggers, even with more stringent parameters ($top_n=20$, $del_n=10$), SOR still cannot effectively mitigate the attacks, maintaining near-perfect ASR. This indicates that defending against dual-sphere attacks requires further increasing top_n or del_n beyond the tested ranges. The enhanced resistance of dual-sphere triggers primarily stems from their implantation of twice as many points as single-sphere triggers, though this comes at the cost of reduced visual stealth due to the larger trigger footprint.

5. Conclusion

This work answers the critical question of how to realize one-to-N backdoor attacks in 3D point clouds by presenting a novel framework centered on configurable spherical triggers. The framework’s feasibility is theoretically established in the Appendix, where our analysis proves that the poisoned model can associate distinct spherical trigger configurations with different target labels based on their spatial properties. This theoretical conclusion is further

validated through rigorous experimentation, demonstrating that multi-target backdoor attacks are not only feasible but pose a severe and flexible threat.

The primary contributions of this work are twofold: first, it establishes the first comprehensive framework for one-to-N backdoor attacks in 3D point clouds, instantiated through two concrete implementations based on configurable spherical triggers; second, it provides extensive experimental validation and theoretical proofs that rigorously confirm the effectiveness of the spherical trigger approaches. These contributions collectively open a new research frontier by proving the viability of parameter configuration as a discriminative mechanism in 3D backdoor attacks, paving the way for even more flexible, stealthy, and defense-resistant one-to-N attacks in 3D domains.

Appendix A. Theoretical Analysis of Spatial Specificity and Spatial Sensitivity

Appendix A.1. Theoretical Foundations

Lemma 1 (Spatial Specificity of Spherical Triggers). *For an insertion-based backdoor attack, let \mathbf{X}'_{R_0} be a poisoned sample created by implanting a spherical trigger S_n at spatial region R_0 , and \mathbf{X}'_{R_1} be created by implanting the same trigger S_n at a spatially non-overlapping region R_1 . Under the Neural Tangent Kernel framework, the predictive probability for target class t_i satisfies:*

$$f_{\theta}(\mathbf{X}'_{R_1})[t_i] < f_{\theta}(\mathbf{X}'_{R_0})[t_i] \quad (\text{A.1})$$

Lemma 2 (Spatial Sensitivity). *Building on Lemma 1, consider an insertion-based backdoor attack with a spherical trigger S_n trained at position R_0 . The predictive probability $f_{\theta}(\mathbf{X}'_R)[t_i]$ exhibits an exponential decay trend with respect to the Euclidean distance $\|R - R_0\|$.*

Appendix A.2. Key Assumptions and Simplifications

The theoretical analysis relies on the following assumptions:

(1) *Kernel Approximation and Similarity Modeling*: We approximate the true NTK using an RBF kernel $K(\mathbf{X}, \mathbf{X}') = \exp(-\gamma\|\Phi(\mathbf{X}) - \Phi(\mathbf{X}')\|^2)$, where $\Phi : \mathbb{R}^{K \times 3} \rightarrow \mathbb{R}^d$ captures essential geometric properties.

(2) *Uniform Class Distribution*: We assume approximately uniform class distribution in benign training data, enabling the simplification $\sum_{j=1}^{H-M} K(\mathbf{X}, \mathbf{X}_j) \cdot \mathbb{I}(y_j = t_i) \approx \sum_{j=1}^{(H-M)/C} K(\mathbf{X}, \mathbf{X}_j)$.

(3) *Small Trigger Assumption*: The spherical trigger S_n is sufficiently small relative to the overall point cloud.

(4) *Local Linearity of Feature Mapping*: The feature mapping Φ is locally Lipschitz continuous around R_0 , satisfying $\|\Phi(\mathbf{X}'(R)) - \Phi(\mathbf{X}'(R_0))\| \leq L \cdot \|R - R_0\| + \mathcal{O}(\|R - R_0\|^2)$.

Appendix A.3. Detailed Proofs

Appendix A.3.1. Proof of Lemma 1

We analyze the poisoned classifier $f_{\theta}(\cdot)$ through kernel regression under the Neural Tangent Kernel theory. The predictive probability for target class t_i is:

$$\varphi_{t_i}(\mathbf{X}) = \frac{\sum_{j=1}^{H-M} K(\mathbf{X}, \mathbf{X}_j) \cdot \mathbb{I}(y_j = t_i) + \sum_{j=1}^M K(\mathbf{X}, \mathbf{X}'_j) \cdot \mathbb{I}(t_j = \mathbf{C}_i(\mathbf{X}'_{R_0}) - A(\mathbf{X}'_{R_0}))}{\sum_{j=1}^{H-M} K(\mathbf{X}, \mathbf{X}_j) + \sum_{j=1}^M K(\mathbf{X}, \mathbf{X}'_j)} > \frac{C(\mathbf{X}'_{R_0}) - A(\mathbf{X}'_{R_0})}{C(\mathbf{X}'_{R_0}) + \epsilon B(\mathbf{X}'_{R_0})} > \frac{C(\mathbf{X}'_{R_0}) - A(\mathbf{X}'_{R_0})}{C(\mathbf{X}'_{R_0}) + B(\mathbf{X}'_{R_0})} \quad (\text{A.2})$$

Assuming uniform class distribution, we simplify to:

$$\varphi_{t_i}(\mathbf{X}) = \frac{\sum_{j=1}^{(H-M)/C} K(\mathbf{X}, \mathbf{X}_j) + \sum_{j=1}^M K(\mathbf{X}, \mathbf{X}'_j)}{\sum_{j=1}^{H-M} K(\mathbf{X}, \mathbf{X}_j) + \sum_{j=1}^M K(\mathbf{X}, \mathbf{X}'_j)} \quad (\text{A.3})$$

We define three key similarity measures:

(1) Similarity to target-class benign samples: $A(\mathbf{X}) = \sum_{j=1}^{(H-M)/C} K(\mathbf{X}, \mathbf{X}_j)$

(2) Similarity to poisoned samples: $B(\mathbf{X}) = \sum_{j=1}^M K(\mathbf{X}, \mathbf{X}'_j)$

(3) Similarity to all benign samples: $C(\mathbf{X}) = \sum_{j=1}^{H-M} K(\mathbf{X}, \mathbf{X}_j)$

Substituting yields:

$$\varphi_{t_i}(\mathbf{X}) = \frac{A(\mathbf{X}) + B(\mathbf{X})}{C(\mathbf{X}) + B(\mathbf{X})} = 1 - \frac{C(\mathbf{X}) - A(\mathbf{X})}{C(\mathbf{X}) + B(\mathbf{X})} \quad (\text{A.4})$$

Consider \mathbf{X}'_{R_0} (trigger at R_0) and \mathbf{X}'_{R_1} (identical trigger at non-overlapping R_1). Due to the spatial non-overlap and the local sensitivity of the feature mapping Φ , the representations differ significantly: $\Phi(\mathbf{X}'_{R_0})$ is not equal to $\Phi(\mathbf{X}'_{R_1})$, leading to reduced similarity to poisoned samples: $K(\mathbf{X}'_{R_1}, \mathbf{X}'_j) < K(\mathbf{X}'_{R_0}, \mathbf{X}'_j)$.

We quantify this similarity reduction with parameter $0 < \epsilon < 1$:

$$B(\mathbf{X}'_{R_1}) \approx \epsilon B(\mathbf{X}'_{R_0}) \quad (\text{A.5})$$

Crucially, for the similarity to benign samples, we leverage the *background invariance* property: since the spherical trigger is small and localized, moving it to a different spatial position R_1 does not significantly alter the overall geometric structure of the point cloud beyond the immediate vicinity of the trigger. Therefore, the similarity to benign samples remains approximately unchanged:

$$A(\mathbf{X}'_{R_1}) \approx A(\mathbf{X}'_{R_0}), \quad C(\mathbf{X}'_{R_1}) \approx C(\mathbf{X}'_{R_0}) \quad (\text{A.6})$$

This background invariance is justified by the small trigger assumption and the local nature of the feature changes induced by trigger displacement.

For \mathbf{X}'_{R_0} :

$$\varphi_{t_i}(\mathbf{X}'_{R_0}) = 1 - \frac{C(\mathbf{X}'_{R_0}) - A(\mathbf{X}'_{R_0})}{C(\mathbf{X}'_{R_0}) + B(\mathbf{X}'_{R_0})} \quad (\text{A.7})$$

For \mathbf{X}'_{R_1} , applying the background invariance and similarity reduction:

$$\varphi_{t_i}(\mathbf{X}'_{R_1}) \approx 1 - \frac{C(\mathbf{X}'_{R_0}) - A(\mathbf{X}'_{R_0})}{C(\mathbf{X}'_{R_0}) + \epsilon B(\mathbf{X}'_{R_0})} \quad (\text{A.8})$$

Since $0 < \epsilon < 1$, we have $C(\mathbf{X}'_{R_0}) + \epsilon B(\mathbf{X}'_{R_0}) < C(\mathbf{X}'_{R_0}) + B(\mathbf{X}'_{R_0})$. With $C(\mathbf{X}'_{R_0}) - A(\mathbf{X}'_{R_0}) > 0$, it follows that:

Therefore:

$$\varphi_{t_i}(\mathbf{X}'_{R_1}) < \varphi_{t_i}(\mathbf{X}'_{R_0}) \quad (\text{A.10})$$

Since $\varphi_{t_i}(\mathbf{X})$ approximates $f_{\theta}(\mathbf{X})[t_i]$ under the NTK framework, we conclude:

$$f_{\theta}(\mathbf{X}'_{R_1})[t_i] < f_{\theta}(\mathbf{X}'_{R_0})[t_i] \quad (\text{A.11})$$

This completes the proof. \square

Appendix A.3.2. Proof of Lemma 2

Proof. Building upon Lemma 1, we analyze the trend of the predictive probability with respect to the distance from the training position R_0 .

From the RBF kernel properties and the local linearity of Φ , the similarity between poisoned samples decays exponentially with distance:

$$\frac{K(\mathbf{X}'_R, \mathbf{X}'_{R_0})}{K(\mathbf{X}'_{R_0}, \mathbf{X}'_{R_0})} \approx \exp(-\gamma L^2 \|R - R_0\|^2) \quad (\text{A.12})$$

where L is the Lipschitz constant of Φ .

This similarity decay affects the poisoned sample similarity term $B(\mathbf{X}'_R)$. Since all poisoned samples for target class t_i are generated with triggers at the fixed position R_0 during training, we have:

$$B(\mathbf{X}'_R) \approx B(\mathbf{X}'_{R_0}) \cdot \exp(-\gamma L^2 \|R - R_0\|^2) + \Delta B(R) \quad (\text{A.13})$$

where $\Delta B(R)$ represents minor variations due to local geometric similarities, which is secondary as established in Lemma 1.

Now, consider the predictive probability under the background invariance assumption (i.e., $C(\mathbf{X}'_R) \approx C(\mathbf{X}'_{R_0})$ and $A(\mathbf{X}'_R) \approx A(\mathbf{X}'_{R_0})$ for small trigger displacements):

$$\varphi_{t_i}(\mathbf{X}'_R) = 1 - \frac{C(\mathbf{X}'_R) - A(\mathbf{X}'_R)}{C(\mathbf{X}'_R) + B(\mathbf{X}'_R)} \approx 1 - \frac{C - A}{C + B(\mathbf{X}'_R)} \quad (\text{A.14})$$

Let $C = C(\mathbf{X}'_{R_0})$, $A = A(\mathbf{X}'_{R_0})$, $B_0 = B(\mathbf{X}'_{R_0})$, and $d = \|R - R_0\|$. The main trend of $\varphi_{t_i}(\mathbf{X}'_R)$ is captured by the function:

$$g(d) = 1 - \frac{C - A}{C + B_0 \cdot \exp(-\gamma L^2 d^2)} = \frac{A + B_0 \exp(-\gamma L^2 d^2)}{C + B_0 \exp(-\gamma L^2 d^2)} \quad (\text{A.15})$$

To rigorously analyze the monotonic behavior, consider the derivative of $g(d)$:

$$g'(d) = -\frac{(C - A)B_0 \cdot 2\gamma L^2 d \cdot \exp(-\gamma L^2 d^2)}{(C + B_0 \exp(-\gamma L^2 d^2))^2} \quad (\text{A.16})$$

Since $C > A > 0$, $B_0 > 0$, $\gamma > 0$, $L > 0$, and $d \geq 0$, we have $g'(d) < 0$ for all $d > 0$, confirming that $g(d)$ is strictly decreasing for $d > 0$. This establishes a decreasing trend. Moreover, as $d \rightarrow \infty$, $g(d) \rightarrow A/C$, and the approach to this baseline is governed by the exponential term, confirming an exponential decay trend.

In practice, due to local variations in $C(\mathbf{X}'_R)$ and $A(\mathbf{X}'_R)$, the predictive probability may not be strictly monotonic. However, the exponential decay trend dominates due to the primary effect of the similarity decay in $B(\mathbf{X}'_R)$, as established by the RBF kernel properties and local linearity assumptions. Since $f_{\theta}(\mathbf{X}'_R)[t_i] \approx \varphi_{t_i}(\mathbf{X}'_R)$ under the NTK framework, the model's predictive probability exhibits an exponential decay trend with respect to $\|R - R_0\|$. \square

Appendix B. Trigger Placement Algorithms

References

- [1] P. Gong and X. Luo, *A survey of video action recognition based on deep learning*, Knowl.-Based Syst., vol. 320, p. 113594, 2025. DOI: 10.1016/j.knosys.2024.113594.
- [2] W. Huang, C. Wang, R. Zhang, Y. Li, J. Wu, and L. Fei-Fei, *VoxPoser: Composable 3D Value Maps for Robotic Manipulation with Language Models*, in *Proceedings of the 7th Conference on Robot Learning (CoRL)*, 2023, pp. 540–562.
- [3] J. Xu, L. Peng, H. Cheng, L. Xia, Q. Zhou, D. Deng, W. Qian, W. Wang, and D. Cai, *Regulating Intermediate 3D Features for Vision-Centric Autonomous Driving*, in *Proceedings of the 38th AAAI Conference on Artificial Intelligence (AAAI)*, 2024, pp. 6306–6314. DOI: 10.1609/aaai.v38i6.28449.

Algorithm 1 Single-Sphere Trigger Placement Algorithm

Input: Number of targets N , candidate set C_a

Output: Set of trigger positions S_e , where each position is a 3D point

- 1: $S_e \leftarrow \{(0.95, 0.95, 0.95)\}$ \triangleright Initialize with fixed point
 - 2: **for** $i \leftarrow 2$ to N **do**
 - 3: $\text{best_point} \leftarrow \emptyset$, $\text{max_min_dist} \leftarrow 0$
 - 4: **for** each $p \in C_a \setminus S$ **do** \triangleright Iterate over candidate points not in S
 - 5: $\text{min_dist} \leftarrow \min_{s \in S} \|p - s\|$ \triangleright Find minimum distance to existing points
 - 6: **if** $\text{min_dist} > \text{max_min_dist}$ **then**
 - 7: $\text{best_point} \leftarrow p$
 - 8: $\text{max_min_dist} \leftarrow \text{min_dist}$
 - 9: **end if**
 - 10: **end for**
 - 11: $S_e \leftarrow S_e \cup \{\text{best_point}\}$ \triangleright Add the best point to the set
 - 12: **end for**
 - 13: **return** S_e
-

Algorithm 2 Dual-Sphere Trigger Placement Algorithm

Input: Number of targets N , candidate set C_{2d} , z-coordinate options $Z = \{0.05, 0.5, 0.95\}$

Output: Set of trigger pairs P , where each pair consists of two points with the same x and y coordinates, and different z coordinates from Z

- 1: $T \leftarrow \{(0.95, 0.95)\}$ \triangleright Initialize with first fixed point
 - 2: **for** $i \leftarrow 2$ to N **do**
 - 3: $\text{best_point} \leftarrow \emptyset$, $\text{max_min_dist} \leftarrow 0$
 - 4: **for** each $q \in C_{2d} \setminus T$ **do** \triangleright Iterate over candidate points not in T
 - 5: $\text{min_dist} \leftarrow \min_{\tau \in T} \|q - \tau\|$ \triangleright Find minimum distance to existing points
 - 6: **if** $\text{min_dist} > \text{max_min_dist}$ **then**
 - 7: $\text{best_point} \leftarrow q$
 - 8: $\text{max_min_dist} \leftarrow \text{min_dist}$
 - 9: **end if**
 - 10: **end for**
 - 11: $T \leftarrow T \cup \{\text{best_point}\}$ \triangleright Add the best point to the set
 - 12: **end for**
 - 13: $P \leftarrow \emptyset$
 - 14: **for** each $(x, y) \in T$ **do**
 - 15: $z_1, z_2 \leftarrow \text{SelectZPair}(Z)$ \triangleright Select two distinct z-coordinates
 - 16: $P \leftarrow P \cup \{(x, y, z_1), (x, y, z_2)\}$ \triangleright Convert to 3D trigger pairs
 - 17: **end for**
 - 18: **return** P
 - 19: **function** $\text{SELECTZPAIR}(Z)$
 - 20: $z_1 \leftarrow \text{RandomChoice}(Z)$
 - 21: $z_2 \leftarrow \text{RandomChoice}(Z \setminus \{z_1\})$ \triangleright Select a different z-coordinate
 - 22: **return** z_1, z_2
 - 23: **end function**
-

- [4] J. Li, H. Li, B. Zhang, Y. Zhang, Y. Wang, and Y. Wang, *PointBA: Towards backdoor attacks in 3D point cloud*, in Proc. IEEE Int. Conf. Comput. Vis. (ICCV), pp. 16472–16481, 2021. DOI: 10.1109/ICCV48922.2021.01614.
- [5] K. Gao, J. Bai, B. Wu, M. Ya, and S.-T. Xia, *Imperceptible and robust backdoor attack in 3D point cloud*, IEEE Trans. Inf. Forensics Security, vol. 19, pp. 1267–1282, 2024. DOI: 10.1109/TIFS.2024.3435198.
- [6] Y. Li, Y. Li, B. Wu, L. Li, R. He, and S. Lyu, *Invisible Backdoor Attack With Sample-Specific Triggers*, in *Proceedings of the IEEE/CVF International Conference on Computer Vision (ICCV)*, 2021, pp. 16443–16452. DOI: 10.1109/ICCV48922.2021.01614.
- [7] M. Xue, C. He, J. Wang, and W. Liu, *One-to-n & n-to-one: Two advanced backdoor attacks against deep learning models*, IEEE Trans. Dependable Secure Comput., vol. 19, no. 3, pp. 1562–1578, 2020. DOI: 10.1109/TDSC.2020.3015409.
- [8] B. Schneider, N. Lukas, and F. Kerschbaum, *Universal backdoor attacks*, in Proc. IEEE/CVF Conf. Comput. Vis. Pattern Recognit. (CVPR), pp. 2345–2354, 2024. DOI: 10.1109/CVPR53160.2024.00843.
- [9] K. D. Doan, Y. Lao, and P. Li, *Marksman backdoor: Backdoor attacks with arbitrary target class*, in Adv. Neural Inf. Process. Syst., vol. 35, pp. 3876–3888, 2022. DOI: 10.48550/arXiv.2206.01213.
- [10] M. Xue, Y. Wu, S. Ni, L. Y. Zhang, Y. Zhang, and W. Liu, *Untargeted backdoor attack against deep neural networks with imperceptible trigger*, IEEE Trans. Inf. Forensics Security, vol. 20, no. 3, pp. 5004–5013, Mar. 2024. DOI: 10.1109/TIFS.2023.3329641.
- [11] Q. Li, W. Chen, X. Xu, Y. Zhang, and L. Wu, *Precision strike: Precise backdoor attack with dynamic trigger*, Comput. Secur., vol. 148, p. 104101, 2025. DOI: 10.1016/j.cose.2024.104101.
- [12] C. R. Qi, H. Su, K. Mo, and L. J. Guibas, *PointNet: Deep learning on point sets for 3D classification and segmentation*, in Proc. IEEE Conf. Comput. Vis. Pattern Recognit., pp. 652–660, 2017. DOI: 10.1109/CVPR.2017.16.
- [13] C. R. Qi, L. Yi, H. Su, and L. J. Guibas, *PointNet++: Deep hierarchical feature learning on point sets in a metric space*, in Adv. Neural Inf. Process. Syst., pp. 5099–5108, 2017. DOI: 10.48550/arXiv.1706.02413.
- [14] Y. Wang, Y. Sun, Z. Liu, S. E. Sarma, M. M. Bronstein, and J. M. Solomon, *Dynamic graph CNN for learning on point clouds*, ACM Trans. Graph., vol. 38, no. 5, pp. 1–12, 2019. DOI: 10.1145/3326362.
- [15] Y. Guo, H. Wang, Q. Hu, H. Liu, L. Liu, and M. Bennamoun, *Deep learning for 3D point clouds: A comprehensive survey*, IEEE Trans. Pattern Anal. Mach. Intell., vol. 46, no. 5, pp. 3218–3238, 2024. DOI: 10.1109/TPAMI.2023.3305436.
- [16] Y. Li, R. Bu, M. Sun, W. Wu, X. Di, and B. Chen, *PointCNN: Convolution on X-transformed points*, in Adv. Neural Inf. Process. Syst., pp. 820–830, 2018. DOI: 10.48550/arXiv.1801.07791.
- [17] W. Wu, Z. Qi, and L. Fuxin, *PointConv: Deep convolutional networks on 3D point clouds*, in Proc. IEEE/CVF Conf. Comput. Vis. Pattern Recognit., pp. 9621–9630, 2019. DOI: 10.1109/CVPR.2019.00985.
- [18] H. Zhao, L. Jiang, J. Jia, P. H. Torr, and V. Koltun, *Point transformer*, in Proc. IEEE/CVF Int. Conf. Comput. Vis., pp. 16259–16268, 2021. DOI: 10.1109/ICCV48922.2021.01594.
- [19] X. Gan, C. Song, J. Li, L. Pan, and K. Xu, *FLPC: Fusing language and point cloud for 3D object classification*, Expert Syst. Appl., vol. 296, p. 128430, 2026. DOI: 10.1016/j.eswa.2024.128430.
- [20] Y.-Z. Feng, S.-H. J. Lin, X. Tang, M.-Y. Wang, J.-Z. Zheng, Z.-Y. He, Z.-Y. Pang, J. Yang, M.-S. Chen, and X. Wei, *Hyperbolic prototype rectification for few-shot 3D point cloud classification*, Pattern Recognit., vol. 158, p. 111042, 2025. DOI: 10.1016/j.patcog.2024.111042.
- [21] T. Gu, B. Dolan-Gavitt, and S. Garg, *BadNets: Identifying vulnerabilities in the machine learning model supply chain*, arXiv preprint arXiv:1708.06733, 2017. DOI: 10.48550/arXiv.1708.06733.
- [22] D. Zhan, K. Xu, X. Liu, T. Han, Z. Pan, and S. Guo, *Practical clean-label backdoor attack against static malware detection*, Comput. Secur., vol. 150, p. 104280, 2025. doi: 10.1016/j.cose.2024.104280.
- [23] C. Liao, H. Zhong, A. Squicciarini, S. Zhu, and D. Miller, *Backdoor embedding in convolutional neural network models via invisible perturbation*, arXiv preprint arXiv:1808.10307, 2018. DOI: 10.48550/arXiv.1808.10307.
- [24] M. Barni, K. Kallas, and B. Tondi, *A new backdoor attack in CNNs by training set corruption without label poisoning*, in Proc. IEEE Int. Conf. Image Process., pp. 101–105, 2019. DOI: 10.1109/ICIP.2019.8803403.
- [25] A. Saha, A. Subramanya, and H. Pirsiavash, *Hidden trigger backdoor attacks*, in Proc. AAAI Conf. Artif. Intell., vol. 34, pp. 11957–11965, 2020. DOI: 10.1609/aaai.v34i07.6749.

- [26] G. Wang, H. Ma, Y. Gao, A. Abuadbbba, Z. Zhang, W. Kang, S. F. Al-Sarawi, G. Zhang, and D. Abbott, *One-to-Multiple Clean-Label Image Camouflage (OmClic) based backdoor attack on deep learning*, *Knowl.-Based Syst.*, vol. 288, p. 111456, 2024. DOI: 10.1016/j.knosys.2024.111456.
- [27] Y. Bian, S. Tian, and X. Liu, *iBA: Backdoor attack on 3D point cloud via reconstructing itself*, *IEEE Trans. Inf. Forensics Security*, vol. 19, pp. 7994–8008, 2024. DOI: 10.1109/TIFS.2024.3435198.
- [28] X. Ning, Q. Xie, J. Xu, W. Jiang, J. Li, and Y. Ma, *Stealthy and robust backdoor attack against 3D point clouds through additional point features*, arXiv preprint arXiv:2412.07511, 2024. DOI: 10.48550/arXiv.2412.07511.
- [29] Y. Gao, H. Chen, W. Zhang, and L. Wang, *A triple stealthy backdoor: Hidden in spatial, frequency, and feature domains*, *IEEE Trans. Dependable Secure Comput.*, vol. 22, no. 1, pp. 456–469, 2025. DOI: 10.1109/TDSC.2025.3496924.
- [30] J. Li, H. Li, B. Zhang, Y. Zhang, Y. Wang, and Y. Wang, *Affinity backdoor attacks in point clouds: A novel method resilient to corruption*, in *Proc. IEEE Int. Conf. Comput. Vis. (ICCV)*, pp. 16482–16491, 2023. DOI: 10.1109/ICCV48922.2023.01587.
- [31] K. Zhang, L. Liu, and W. Wang, *MirrorAttack: Backdoor attack on 3D point cloud with a distorting mirror*, in *Proc. AAAI Conf. Artif. Intell.*, vol. 38, no. 8, pp. 9234–9242, 2024. DOI: 10.1609/aaai.v38i8.28745.
- [32] L. Fan, F. He, T. Si, W. Tang, and B. Li, *Invisible backdoor attack against 3D point cloud classifier in graph spectral domain*, in *Proc. AAAI Conf. Artif. Intell.*, vol. 38, no. 11, pp. 11867–11875, 2024. DOI: 10.1609/aaai.v38i11.29177.
- [33] Y. Cai, Y. Zhang, Z. Wang, and L. Chen, *A method and device for adversarial attack on 3D point cloud object tracking based on frequency domain importance*, CN Patent 119006518A, 2024.
- [34] X. Liu, Y. Wang, Y. Tan, K. Qiu, and Y. Li, *Point cloud attack in graph spectral domain: When 3D geometry meets graph signal processing*, *IEEE Trans. Pattern Anal. Mach. Intell.*, vol. 46, no. 5, pp. 3218–3238, 2024. DOI: 10.1109/TPAMI.2023.3305436.
- [35] H. Zhou, K. Chen, W. Zhang, H. Fang, W. Zhou, and N. Yu, *Dup-net: Denoiser and upsampler network for 3D adversarial point clouds defense*, in *Proc. IEEE/CVF Int. Conf. Comput. Vis.*, pp. 1961–1970, 2019. DOI: 10.1109/ICCV.2019.00205.
- [36] C. Wei, Y. Wang, K. Gao, S. Shao, Y. Li, Z. Wang, and Z. Qin, *PointNCBW: Towards dataset ownership verification for point clouds via negative clean-label backdoor watermark*, *IEEE Trans. Inf. Forensics Security*, vol. 20, pp. 1234–1248, 2025. DOI: 10.1109/TIFS.2025.3490703.
- [37] Z. Wu, S. Song, A. Khosla, F. Yu, L. Zhang, X. Tang, and J. Xiao, *3D ShapeNets: A deep representation for volumetric shapes*, in *Proc. IEEE Conf. Comput. Vis. Pattern Recognit.*, pp. 1912–1920, 2015. DOI: 10.1109/CVPR.2015.7298838.
- [38] L. Yi, V. G. Kim, D. Ceylan, I.-C. Shen, M. Yan, H. Su, C. Lu, Q. Huang, A. Sheffer, and L. Guibas, *A scalable active framework for region annotation in 3D shape collections*, *ACM Trans. Graph.*, vol. 35, no. 6, pp. 1–12, 2026. DOI: 10.1145/2988450.2988459.
- [39] H. Zhao, L. Jiang, J. Jia, P. H. Torr, and V. Koltun, *Point transformer*, in *Proc. IEEE/CVF Int. Conf. Comput. Vis.*, pp. 16259–16268, 2021. DOI: 10.1109/ICCV48922.2021.01594.
- [40] H. Zhou, K. Chen, W. Zhang, H. Fang, W. Zhou, and N. Yu, *Dup-net: Denoiser and upsampler network for 3D adversarial point clouds defense*, in *Proc. IEEE/CVF Int. Conf. Comput. Vis.*, pp. 1961–1970, 2019. DOI: 10.1109/ICCV.2019.00205.